Changing intensity of hydroclimatic extreme events revealed by GRACE and GRACE-FO

Authors:

Matthew Rodell[1] and Bailing Li[1,2]

[1] NASA Goddard Space Flight Center, Greenbelt, Maryland, USA
[2] University of Maryland, College Park, Maryland, USA

Corresponding Author:

Matthew Rodell
+1 301-286-9143
Matthew.Rodell@nasa.gov

Final Revision, 2 February 2023

Abstract

Distortion of the water cycle, particularly of its extremes (droughts and pluvials), will be among the most conspicuous consequences of climate change. We applied a novel approach with terrestrial water storage observations from the GRACE and GRACE-FO satellites to delineate and characterize 1,056 extreme events during 2002-2021. Dwarfing all other events was an ongoing pluvial that began in 2019 and engulfed central Africa. Total intensity of extreme events was strongly correlated with global mean temperature, more so than with the El Nino Southern Oscillation or other climate indicators, suggesting that continued warming of the planet will cause more frequent, more severe, longer, and/or larger droughts and pluvials. In three regions, including a vast swath extending from southern Europe to southwestern China, the ratio of wet to dry extreme events decreased substantially over the study period, while the opposite was true in two regions, including sub-Saharan Africa from 5°N to 20°N.

Main Text

Floods and droughts account for more than 20% of the economic losses caused by extreme weather events in the U.S. each year, ranked 2nd following hurricanes among all major disasters (https://www.drought.gov/news/high-cost-drought), and their human toll is most devastating in poor and developing nations[1]. Numerous publications describe the latest theories on how the water cycle and its extremes are being modulated by climate change[2–9]. However, suspected systematic, continental to global changes in hydrological extremes are difficult to verify[10,11]. Such verification and better quantification of how the frequency and intensity of hydrological extremes may be responding to climate change would be valuable for improving preparedness, mitigating impacts, and communicating the urgency of the current situation.

Many previous large-scale studies of water storage variations during droughts and pluvials (periods with relatively large amounts of precipitation, i.e., the opposite of droughts) focused on soil moisture and snow and were conducted using hydrological models[12–14]. However, such models contain considerable uncertainty due to deficiencies in their input data and simplified physics[15–17]. For example, atmospheric re-analysis-products frequently used to drive hydrological models are prone to underestimating extreme precipitation[18] and are subject to large uncertainties at high elevations and during snow events[19] and, therefore, are likely to misrepresent the occurrence and severity of floods.

We applied satellite gravimetry based observations of terrestrial water storage (TWS) anomalies[20] from the Gravity Recovery and Climate Experiment[21] (GRACE) and GRACE Follow-On[22] (GRACE-FO) satellite missions (hereafter GRACE/FO) to study hydrological extremes and their extent, frequency, and duration during 2002-2021. Because GRACE/FO measures water storage changes in the entire vertical profile, it provides a more complete quantification of hydrological response to extreme events than do other types of observations. The efficacy of GRACE/FO in detecting and quantifying water cycle extremes has been demonstrated in numerous contexts[23–34]. We employed an objective, spatial-temporal clustering algorithm[35] to identify contiguous regions experiencing wet/dry extreme conditions without pre-defined boundaries (see Methods). It yielded 505 wet clusters and 551 dry clusters (excluding those that fell entirely in the GRACE/FO gap period; Table 1). About 70% of the events lasted 6 months or less and about 10% of them lasted 12 months or more, with average durations of 5 to 6 months (Table 1). We ranked the most intense events in each continent and globally, determined using an intensity metric[32] that is based on spatially and temporally accumulated TWS anomalies.

Results

The most intense wet and dry events

The intensity metric integrates three aspects of an event: TWS anomaly (equivalent height of water), horizontal extent, and duration. Hydrological extremes evaluated using TWS differ from those based on accumulated precipitation, soil moisture, or streamflow data. Specifically, TWS has a wider range of variability than soil moisture, its anomalies are commonly more persistent than those of either soil moisture or streamflow, and it represents the combined effects of all hydrological fluxes[36]. The seven most intense wet and dry events during the study period are mapped in Figure 1, along with time series showing how their TWS anomalies evolved. The overall most intense extreme water cycle event since 2002 was a 31,354 km^3mo pluvial covering most of sub-Saharan Africa above 10°S. This event caused Lake Victoria to rise by over 1 m, with flooding in the surrounding region[37]. Remarkably, it was ongoing as of December 2021 and dwarfed the next most intense event, a 11,896 km^3mo pluvial covering much of central and eastern North America[38] during 2018-2021. The third most intense wet event (10,713 km^3mo) occurred in Australia during 2011-2012 and is notable both for ending the Millennium Drought[33] and for causing sea level briefly to decline[24]. The most intense dry event (-10,513 km^3mo) observed by GRACE/FO was a short but severe, record-breaking drought[39] in northeastern South America during 2015-2016. A 2019-present drought (-6,245 km^3mo) that encompasses the Cerrado region of Brazil threatens hydroelectric power production[40] and may soon become the second most intense dry event in the GRACE/FO record. Similarly, the ongoing drought in southwestern North America (-4,557 km^3mo) has caused water levels in two of the biggest reservoirs in the U.S., Lakes Mead and Powell, to decline to dangerously low levels[41]. A pan-European dry event (-5,689 km^3mo) briefly ended in 2021 based on our criteria, but water levels remained below normal and the drought reignited in 2022, causing several rivers to approach historic lows and straining energy supplies[42]. A 2009 pluvial (7,260 km^3mo) in the Amazon[25] that caused major flooding also appears in Figure 1. Figures ED1 and ED2 map the top 30 wet and top 30 dry events as the fraction of time during which each grid cell experienced wet/dry conditions during the period of the event. Among other historic events, the 2012 drought (-4,098 km^3mo) that affected most of the contiguous U.S.[43] ranked as the tenth most intense dry event. Australia's Millennium Drought[33] was identified by the clustering algorithm as three smaller events (not ranked in the top 30), which, taken together, would have ranked as the 14th most intense drought.

On the whole, there were nearly 10% more dry (551) than wet (505) events identified by the clustering algorithm (a difference significant at the 99.5% confidence level, based on Chi-squared testing), while average event extent and duration were similar between the two types of events, both for the 30 most intense events and overall (Table 1). On the other hand, only two dry events exceeded magnitude 7,000 km^3mo, whereas four wet events did so, including three that exceeded 10,000 km^3mo and one three times that size. At the end of the study period, major extreme events were ongoing in central Africa (31,354 km^3mo), southern Africa (5,199 km^3mo), southern Brazil (-6,245 km^3mo), and southwestern North America (-4,557 km^3mo), which were four of the 14 most intense events in the 19-year record, and that's not including the revived drought in Europe. As discussed below, the global total intensity of major extreme events appears to be increasing as the world warms.

Hydroclimatic variability and change

To investigate interannual variability and drivers of extreme TWS events, we examined changes in worldwide intensity and other extreme event metrics during the study period, and their relationships with hydroclimatic oscillations and indicators. Prior to 2019, total monthly intensity (the sum of the absolute values of the inner integral of equation 1 over all active dry and wet events) remained within a well-defined range, about 400 to 2,600 km^3mo, before rapidly increasing to a high of 4,900 km^3mo in 2021 (Figure 2). The El Niño Southern Oscillation (ENSO) had an apparent influence, with the maximum TWS anomalies of the top 3 wet events having occurred in either La Niña or El Niño years (shaded in gray in Figure 2) and the minimum TWS anomaly of the top dry event having occurred in an El Niño year. In addition, the warmest seven years in the meteorological data record, at the time of writing, were 2015-2021. During that period, the frequency of the most extreme (top 30 wet and top 30 dry) events was 4 per year, compared with 3 per year in the previous 13 years. Global monthly total dry and wet event intensities were significantly correlated (r = -0.57 and r = 0.63) with global mean temperature (a negative correlation indicates that events become drier with rising temperature). The number and average severity of dry events, assessed at the global scale, were even better correlated (r = 0.64 and r = -0.74 at 0- and 11-month lags) with global mean temperature, and average duration and total extent were also well correlated (r = 0.51 at 12-month lag and r = 0.43 unlagged). Similarly, global mean temperature was well correlated with wet event average severity (r = 0.58 at 12-month lag), average duration (r = 0.47 at 11-month lag), and total extent (r = 0.60 at 12-month lag). All of these correlation coefficients (which are compiled in Table ED1) are significant at the 0.95 confidence level.

Beyond significance testing, to assess the robustness of the apparent linkage between global mean temperature and extreme hydroclimatic events, we computed correlations among the same five extreme event metrics and six major climate indices that are known to modulate terrestrial hydroclimate including TWS[44–46]: the Southern Oscillation Index (SOI; an ENSO indicator), the Trans Nino Index (TNI), the Pacific Decadal Oscillation (PDO), the North Atlantic Oscillation (NAO), the Atlantic Multidecadal Oscillation (AMO), and the Dipole Mode Index (DMI). Of the 60 resulting dry and wet event correlation coefficients, only one exceeded 0.50: average duration of wet events vs. DMI (r = 0.55 unlagged). Five others exceeded 0.40, including total wet event intensity vs. DMI (r = 0.41 at 12-month lag), while the majority were much lower. Despite the oft-presumed dominance of ENSO, the largest correlation coefficient between SOI and any wet or dry event metric was 0.29 (4-month lag) with wet event total intensity. Taken together, these results suggest that rising temperatures may be driving an increase in the total intensity and related metrics of hydroclimatic extreme events that cannot be attributed to the sporadic occurrence of ENSO or other climate oscillations. While causation remains unproven, it would be counterintuitive for extreme water cycle events to drive global mean temperature, and it is unlikely that the catalyst of temperature increase, greenhouse gas accumulation, would effect hydroclimatic extreme events directly. On the other hand, warmer air boosts evaporative demand during dry events[47] while raising the amount of atmospheric moisture available (i.e., imported from the ocean or other regions) to fuel wet events[48], perhaps leading to an intensification of the water cycle and increased TWS variability[49,50].

Figure 3 illustrates how the evident effects of global warming on extreme event intensity vary across the four Köppen-Geiger climate zones. The largest overall correlations were between global mean temperature and monthly wet event intensity in tropical and continental climates (both r = 0.67 at 11- and 12-month lags). Wet events in the tropical zone had by far the greatest mean TWS anomalies of the four climates (Table ED2). In the continental zone, duration is a bigger component of wet event intensity than in the other zones. In dry climates, the influence of global temperature on wet event intensity was insignificant, while other climate oscillations were bigger factors, including SOI (r = 0.62 at 5-month lag) and NAO (-0.57 at 12-month lag). The largest global temperature correlations with dry event intensity were found in tropical climates (r = -0.64 unlagged; Figure 3), which makes sense because high temperatures increase actual ET where it is energy limited, as is often the case in tropical regions. The overall most intense dry event occurred in the Amazon, a tropical climate, during the hottest year, 2016, thus likely contributing to the strong correlation. Even more so than with wet events, TWS anomalies of dry events in tropical regions dwarfed those in other climates (Table ED3), reflecting the large dynamic range of TWS in wet tropical regions. However, the correlation between intensity and global temperature in dry climates was also large (r = -

0.61 at 12-month lag), which supports half of the "wet-gets-wetter, dry-gets-drier" (WWDD) hypothesis of hydroclimatic change[51]. Event duration appears to be an important component of intensity in dry regions (Table ED3).

Certain geographical regions exhibited coherence of changing frequency of wet and dry extreme events. Figure 4 shows the location, year of maximum TWS anomaly, and intensity of the 551 dry and 505 wet events. Five polygons delineate regions of coherence. In southwestern North America, the frequency of wet events decreased while most dry events occurred during the second half of the study period (see also Figure ED3). The series of droughts in the southwestern U.S. after 2012, exacerbated by groundwater pumping to support irrigated agriculture, is well documented[52]. Clear shifts from a preponderance of wet events to predominantly dry events are also apparent in southeastern Brazil and within a vast swath from southern Europe across the Middle East and Arabian Peninsula to southwestern China and Bangladesh. The tendencies in southwestern North America and southeastern Brazil generally corroborate IPCC AR6 predictions of precipitation change (recognizing that extreme hydroclimatic event occurrence and precipitation are related but not equivalent), while the tendency in the Arabian Peninsula partly contradicts them: IPCC AR6 predicts increased precipitation there[11]. In sub-Saharan Africa and west central South America, there were more dry events in the first half of the period and more wet events in the second half. The former tendency is consistent with the IPCC AR6 consensus prediction of large percentage increases in precipitation across most of northern Africa, but the latter is inconsistent with them. There were not enough events in every polygon to perform statistically significant correlation analyses with global mean surface temperature, but the tendencies suggest that the first group is responding to global warming with more (and greater total intensity of) dry events and fewer (smaller total intensity of) wet events, and vice versa in the other two regions.

Considering ENSO's well established influence on global precipitation patterns[53], it is worthwhile to evaluate its relationship with extreme event tendencies in these five regions. La Nina dominated the second quarter of the study period and also the last two years (Figure 2). The only strong El Nino occurred in 2015-2016, i.e., about midway through the second half of the study period. Thus, we might expect a general trend from La Nina to El Nino type wetness conditions in regions where a teleconnection has been documented, if ENSO is, in fact, a dominant driver of extreme events. Both Sub-Saharan Africa and northern South America are known to receive more rainfall during La Nina than during El Nino[54]. However, dry events dominated the first half of the study period and wet events dominated the second half (Figure 4), suggesting that something other than ENSO controlled extreme hydroclimatic event frequency during the study period in these two regions. In the southwestern U.S. and northern Mexico, more rainfall typically occurs during El Nino than during La Nina[54]. However, the first half of the period was dominated by extreme wet events while extreme dry events dominated the second half in this region, again suggesting that ENSO was not the primary driver. In the other regions outlined in Figure 4, the effects of ENSO were more ambiguous.

Figure 4 also displays the zonal average years of occurrence for wet and dry events. In the equatorial region (15°S to 15°N), wet events occurred more frequently and dry events less frequently towards the end of the study period. The opposite was true in the northern mid-latitudes (15°N to 50°N). Noting the general trend of global warming during the period (Figure 2), these tendencies support the WWDD hypothesis. Tendencies in other latitude bands were equivocal.

Discussion

With a data record that exceeds 20 years, GRACE and GRACE-FO enable identification and quantification of extreme hydroclimatic events globally, in terms of TWS anomalies and associated metrics, that were not previously possible. For decades, precipitation data have served as the basis for a majority of investigations of water cycle extremes, though observations of surface waters, soil moisture, and evapotranspiration are also employed[55]. Because they integrate the effects of precipitation, runoff, and ET (which itself has multiple controls), TWS data and the intensity metric in particular enable a more holistic understanding of hydroclimatic extreme event depth, extent, and duration. Making use of these data and a novel clustering algorithm, we have presented a new ranking of the most intense water cycle events of the past two decades. The approach is reproducible, so that ongoing and future extreme events can continue to be delineated and assessed, making use of data from GRACE-FO and its proposed successor, the Mass Change mission[56]. This will be important given our finding that global monthly intensity of extreme hydroclimatic events is increasing as the world warms, which is consistent with the Intergovernmental Panel on Climate Change Sixth Assessment Report's medium-to-high confidence conclusion that the severity (defined differently) of extreme water cycle events is increasing[11]. About one third of the global top 30 wet and top 30 dry events were located in South America, which is logical considering the relative strength and variability of its water cycle[57]. The most intense extreme events increased from about 3 to 4 per year after

2015, just as global temperatures began to hit a series of record or near-record highs. A tendency towards more wet events and fewer dry events was observed in the equatorial region (15°S – 15°N). In contrast, between 15°N and 50°N the number of dry events increased in the latter half of the study period while the number of wet events decreased, which is concerning in the context of future freshwater availability (but positive from a flood hazard perspective) because roughly half of the world's population lives in that zone. If this portends a drier future, there could be dire consequences for human health, food security, human migration, and regional unrest and conflict.

Methods

We used GRACE/FO products developed by the Center for Space Research (CSR) at the University of Texas[20] in our analyses. The products were generated using a mass concentration (mascon) technique, constrained with a time-variable regularization matrix based on GRACE/FO information only during the derivation of gravity fields from satellite ranging measurements. This approach better preserves GRACE/FO signals as it eliminates the need for the type of postprocessing required by the spherical harmonic method[20,58]. The CSR data were provided on a 0.25° global grid, which facilitated separation of the ocean and land signals. However, the effective spatial resolution is significantly coarser due to the limitations of the observing technique and instruments: around 150,000 km^2 at mid-latitudes[59,60]. Although GRACE began collecting observations in April 2002, the April and May 2002 data are highly uncertain due to instrument calibration, and June and July 2002 data are missing. Therefore, we used GRACE/FO data from August 2002 to December 2021 in this study.

Because long-term trends can cause misidentification of extreme events, we excluded regions that are known to be experiencing anthropogenic groundwater depletion. These included California's Central Valley, Northern India, and the North China Plain[61]. Greenland, the Gulf of Alaska, and Patagonia, where ice sheet and glacier ablation have caused significant TWS decreases, were also excluded. Our delineation of these regions followed an earlier study[61].

The 11-month gap (July 2017 to May 2018) between the GRACE and GRACE-FO missions and 18 additional missing months of data were filled using TWS output from a global GRACE/FO data assimilating instance[62] of the Catchment land surface model[63] (CLSM). CLSM-simulated TWS comprises soil moisture, groundwater, snow water equivalent, and canopy interception water storage. CLSM does not simulate surface water or permanent ice, whose changes are detected by GRACE/FO. The lack of simulated surface water is unlikely to have a significant effect on our results because CLSM effectively carries surface water as additional groundwater (in the real world, the two are sometimes considered to be a single resource[64]). Further, only 29 of the 233 months of the study period relied on data assimilation output. Regions with permanent ice cover were excluded from the analysis, as previously stated. Due to CLSM's inability to simulate groundwater extraction, it may underestimate TWS dynamics in regions where groundwater withdrawals exacerbate TWS losses during droughts. By excluding regions with secular trends due to groundwater depletion and by filling only short gaps, we have already minimized that potential source of error. Nevertheless, considering these limitations and the fact that CLSM-simulated TWS is less effectively constrained during the 11-month gap period, we excluded from our analysis any extreme events (described below) that occurred entirely within that gap period.

Due to our focus on large extreme events and considering the coarse effective resolution of GRACE/FO observations, we first aggregated the 0.25° CSR data (with gaps filled by TWS from the GRACE/FO data assimilation simulation) to a 2° grid, which balances the effective resolution with our ability to define regions satisfactorily. For a given month in any 2° grid cell, wet or dry conditions were flagged if the standardized TWS anomaly (based on the location-specific mean and standard deviation) was greater than one or less than negative one (thereafter this is referred to as the one-σ threshold), respectively. Assuming a normal distribution, the one-σ threshold yields wet or dry conditions 16% of the time. Based on the drought categories of the U.S. Drought Monitor[65], dry conditions identified with the one-σ threshold encompass exceptional, extreme, and severe droughts and some moderate droughts.

The ST-DBSCAN spatial and temporal clustering algorithm[35] was used to amalgamate contiguous, flagged, wet and dry data points into wet and dry events. Wet events only comprise wet points and dry events only comprise dry points. ST-DBSCAN employs a spatial radius (R) and a time interval to define a search domain around a wet/dry cell. Because extreme events are naturally contiguous in space and time, we set R to 250 km, which is long enough to span two adjacent 2° grid cells at the equator, and we set a one-month interval, so that wet or dry cells from the two months adjacent to the current month were included in the search domain. A minimum number of neighboring data points (N_{min}) determines if a cell should be identified as a core point and given a cluster label. The process repeats for all cells neighboring the core point, and any neighboring core points receive the same cluster label. We confirmed that R=250 km and a one-month interval, N_{min}=12 yielded an optimal set of clusters by examining intra-clustering distance, the averaged distance of all wet/dry cells to the centroid of a cluster, and inter-cluster distance, the distance between the centroids of two clusters.

In our analyses, wet or dry severity at a grid cell was defined as the standardized (divided by the temporal standard deviation) TWS anomaly, and the severity of an event was computed as the average severity over all cells currently exceeding the one-σ threshold. The intensity (km^3mo) of a given event, *I*, was defined[32] as the sum of the individual wet/dry grid cell TWS anomalies (cm equivalent height of water converted to km) multiplied by the associated grid cell areas (km^2), summed over the duration (months):

$$I = \sum_{j=1}^{T}\sum_{i=1}^{M} A_{ij}Y_{ij} \qquad (1)$$

where A_{ij} and Y_{ij} are the cell area and seasonal TWS anomaly (equivalent height of water relative to the long term mean for that month and location) at grid cell i and time j; M is the total number of dry or wet cells at time j; and T is the duration (number of months) of an event. Hence, intensity is a hydroclimatic event metric that incorporates water surplus or deficit (TWS anomaly), duration, and extent. Naturally, intensity is positive for wet events and negative for dry events.

Global characteristics (number, intensity, extent, duration, and severity) of extreme wet and dry events were calculated by summing (intensity and extent), averaging (severity and duration), or counting (number) over all active events. As needed, the timing of an individual event (e.g., Figures 2 & 4) was determined based on the month of the maximum absolute, non-seasonal TWS anomaly (km^3). The location where an event persisted longest determined the climate class to which it belonged (Figures ED1 and ED2). All correlations were computed as standard Pearson correlation coefficients and significance was determined using the t-statistic,

$$t = r\sqrt{(N-2)/(1-r^2)} \qquad (2)$$

where r is the correlation coefficient and N is the number of samples in the time series. The monthly seasonal cycle was removed from the global mean temperature (GISTemp) time series prior to computing correlation coefficients. In Figure 2, the GISTemp time series was smoothed using 6-month sliding window averaging, but smoothing was not applied prior to the correlation analysis.

Data Availability

The GRACE/FO products (CSR GRACE/GRACE-FO RL06 Mascon Solutions, version 02) used in our analyses are available from the University of Texas Center for Space Research (https://www2.csr.utexas.edu/grace/RL06_mascons.html). The output from a global GRACE/FO data assimilating instance of the Catchment land surface model (GRACEDADM_CLSM025GL_7D 3.0) used to fill the 11-month gap between the GRACE and GRACE-FO missions and 18 additional missing months is available from the Goddard Earth Sciences Data and Information Services Center (https://disc.gsfc.nasa.gov/datasets/GRACEDADM_CLSM025GL_7D_3.0/). The climate oscillation indicator data can be downloaded from the NOAA Physical Sciences Laboratory (https://psl.noaa.gov/data/climateindices/list/ and https://psl.noaa.gov/gcos_wgsp/Timeseries/DMI/). The global mean temperature data are available from the NASA Goddard Institute for Space Studies (https://data.giss.nasa.gov/gistemp/). Köppen-Geiger climate map data are available for download from http://koeppen-geiger.vu-wien.ac.at/present.htm. Key data[66] including those used to create the four main text figures are available from https://doi.org/10.5281/zenodo.7599831.

Code Availability

The python code for the ST-DBSCAN clustering algorithm was obtained from the Github repository, https://github.com/gitAtila/ST-DBSCAN. Statistical analyses were performed and figures were generated using NCL software.

Acknowledgements

This study was funded by NASA's GRACE-FO Science Team and NASA's Energy and Water Cycle Study (NEWS) program. Computing resources supporting this work were provided by NASA's High-End Computing (HEC) Program through the NASA Center for Climate Simulation (NCCS) at Goddard Space Flight Center. GRACE and GRACE-FO were jointly developed and operated by NASA, DLR, and the GFZ German Research Centre for Geosciences.

Author Contributions

M.R. designed the study with input from B.L. B.L. led the clustering, correlation, and uncertainty analyses with input from M.R. M.R. designed the figures and B.L. created them. M.R. and B.L. discussed the results and wrote the manuscript.

Competing Interests

The authors claim no competing interests.

Tables

	continent	number of events	average extent (max extent, 10^6 km^2)	average duration (max duration, months)
wet events	Eurasia	239	0.38 (2.3)	6 (39)
	North America	122	0.33 (2.8)	6 (33)
	South America	66	0.53 (2.4)	6 (20)
	Africa	56	0.52 (7.8)	5 (34)
	Australia	22	0.58 (3.9)	6 (33)
dry events	Eurasia	266	0.35(3.0)	6 (34)
	North America	112	0.34 (2.6)	6 (43)
	South America	77	0.47 (2.8)	6 (22)
	Africa	65	0.56 (2.6)	6 (25)
	Australia	31	0.49 (1.6)	5 (11)

Table 1. Summary of wet and dry events in five continents.

Figure Captions

Figure 1. The most intense wet and dry events. Spatial extents of (a) the top seven most intense wet and (b) the top seven most intense dry events globally and the associated TWS anomaly (km^3) time series (color coded). The intensity (km^{3}mo) of an event is equivalent to the integral under its time series.

Figure 2. Relationships between the extreme events, ENSO, and global surface temperature. Intensity (10^3 km^3mo) of the global top 30 most intense wet (positive values) and top 30 most intense dry (negative values) events (dots color coded by continent) as a function of the month of maximum/minimum TWS anomaly. The dashed line indicates monthly total intensity (sum of the absolute value of monthly TWS anomalies of all active events). Dark shading indicates an El Nino period and light shading indicates a La Nina period. Plotted below is the time series of global mean surface temperature anomalies (Celsius) from the Goddard Institute for Space Studies (GISTemp).

Figure 3. Correlations between extreme event total intensity and global mean temperature by climate zone. (a) Map of the four major Köppen-Geiger climate zones, (b) maximum 0-12 month lagged correlations between monthly global mean temperature and total wet (blue) and dry (red) event intensity within each climate zone. A negative correlation indicates that absolute intensity of dry (wet) events increases (decreases) with rising temperature.

Figure 4. Regional coherence of extreme event timing. Map of wet (top panel; 505 events) and dry (bottom panel; 551 events) event occurrence, defined by the year of maximum absolute TWS anomaly (km^3). The location indicates the cell where the event remained longest. The blue polygons delineate five regions where there is general consistency in the type of event (wet/dry) in the two halves of the study period. The zonal average year of occurrence (right) was smoothed with a 6° moving window.

References

1. Miyan, M. A. Droughts in Asian least developed countries: Vulnerability and sustainability. *Weather Clim Extrem* **7**, 8–23 (2015).

2. Bishop, D. A., Williams, A. P. & Seager, R. Increased Fall Precipitation in the Southeastern United States Driven by Higher-Intensity, Frontal Precipitation. *Geophys Res Lett* **46**, 8300–8309 (2019).

3. Blöschl, G. *et al.* Changing climate both increases and decreases European river floods. *Nature* **573**, 108–111 (2019).

4. Du, H. *et al.* Precipitation from Persistent Extremes is Increasing in Most Regions and Globally. *Geophys Res Lett* **46**, 6041–6049 (2019).

5. Martin, J. T. *et al.* Increased drought severity tracks warming in the United States' largest river basin. *Proc Natl Acad Sci USA* **117**, 11328–11336 (2020).

6. Papalexiou, S. M. & Montanari, A. Global and Regional Increase of Precipitation Extremes Under Global Warming. *Water Resour Res* **55**, 4901–4914 (2019).

7. Williams, A. P. *et al.* Contribution of anthropogenic warming to California drought during 2012-2014. *Geophys Res Lett* **42**, 6819–6828 (2015).

8. Ye, H. & Fetzer, E. J. Asymmetrical Shift Toward Longer Dry Spells Associated with Warming Temperatures During Russian Summers. *Geophys Res Lett* **46**, 11455–11462 (2019).

9. Zolotokrylin, A. N. & Cherenkova, E. A. Seasonal changes in precipitation extremes in Russia for the last several decades and their impact on vital activities of the human population. *Geography, Environment, Sustainability* **10**, 69–82 (2017).

10. U.S. Global Change Research Program. *Impacts, Risks, and Adaptation in the United States: The Fourth National Climate Assessment, Volume II*. https://nca2018.globalchange.gov/ (2018) doi:10.7930/NCA4.2018.

11. Douville, H. *et al.* Water Cycle Changes Supplementary Material. in *Climate Change 2021: The Physical Science Basis. Contribution of Working Group I to the Sixth Assessment Report of the Intergovernmental Panel on Climate Change* (eds. of Working Group I. to the Sixth Assessment Report of the Intergovernmental Panel on Climate Change [Masson-Delmotte, C. et al.) (Cambridge University Press, 2021).

12. Andreadis, K. M., Clark, E. A., Wood, A. W., Hamlet, A. F. & Lettenmaier, D. P. Twentieth-century drought in the conterminous United States. *J Hydrometeorol* **6**, 985–1001 (2005).

13. Sheffield, J., Andreadis, K. M., Wood, E. F. & Lettenmaier, D. P. Global and continental drought in the second half of the twentieth century: Severity-area-duration analysis and temporal variability of large-scale events. *J Clim* **22**, 1962–1981 (2009).

14. He, X., Pan, M., Wei, Z., Wood, E. F. & Sheffield, J. A global drought and flood catalogue from 1950 to 2016. *Bull Am Meteorol Soc* **101**, E508–E535 (2020).

15. Kato, H. *et al.* Sensitivity of land surface simulations to model physics, land characteristics, and forcings, at four CEOP sites. *Journal of the Meteorological Society of Japan* **85 A**, 187–204 (2007).

16. Xia, Y. *et al.* Comparison and assessment of three advanced land surface models in simulating terrestrial water storage components over the United States. *J Hydrometeorol* **18**, 625-649 (2017).

17. Scanlon, B. R. *et al.* Global models underestimate large decadal declining and rising water storage trends relative to GRACE satellite data. *Proc Natl Acad Sci U S A* **115**, E1080–E1089 (2018).

18. Hu, G. & Franzke, C. L. E. Evaluation of Daily Precipitation Extremes in Reanalysis and Gridded Observation-Based Data Sets Over Germany. *Geophys Res Lett* **47**, e2020GL08962 (2020).

19. Cui, W., Dong, X., Xi, B. & Kennedy, A. Evaluation of reanalyzed precipitation variability and trends using the gridded gauge-based analysis over the CONUS. *J Hydrometeorol* **18**, 2227–2248 (2017).

20. Save, H., Bettadpur, S. & Tapley, B. D. High-resolution CSR GRACE RL05 mascons. *J Geophys Res Solid Earth* **121**, 7547–7569 (2016).

21. Tapley, B. D., Bettadpur, S., Watkins, M. & Reigber, C. The gravity recovery and climate experiment: Mission overview and early results. *Geophys Res Lett* **31**, L09607 (2004).

22. Landerer, F. W. *et al.* Extending the Global Mass Change Data Record: GRACE Follow-On Instrument and Science Data Performance. *Geophys Res Lett* **47**, e2020GL088306 (2020).

23. Andersen, O. B., Seneviratne, S. I., Hinderer, J. & Viterbo, P. GRACE-derived terrestrial water storage depletion associated with the 2003 European heat wave. *Geophys Res Lett* **32**, L18405 (2005).

24. Boening, C., Willis, J. K., Landerer, F. W., Nerem, R. S. & Fasullo, J. The 2011 la Nia: So strong, the oceans fell. *Geophys Res Lett* **39**, L19602 (2012).

25. Chen, J. L., Wilson, C. R. & Tapley, B. D. The 2009 exceptional Amazon flood and interannual terrestrial water storage change observed by GRACE. *Water Resour Res* **46**, W12526 (2010).

26. Getirana, A. Extreme water deficit in Brazil detected from space. *J Hydrometeorol* **17**, 591–599 (2016).

27. Leblanc, M. J., Tregoning, P., Ramillien, G., Tweed, S. O. & Fakes, A. Basin-scale, integrated observations of the early 21st century multiyear drought in Southeast Australia. *Water Resour Res* **45**, W04408 (2009).

28. Reager, J. T., Thomas, B. F. & Famiglietti, J. S. River basin flood potential inferred using GRACE gravity observations at several months lead time. *Nat Geosci* **7**, 588–592 (2014).

29. Shah, D. & Mishra, V. Strong Influence of Changes in Terrestrial Water Storage on Flood Potential in India. *Journal of Geophysical Research: Atmospheres* **126**, e2020JD033566 (2021).

30. Singh, A., Reager, J. T. & Behrangi, A. Estimation of hydrological drought recovery based on precipitation and Gravity Recovery and Climate Experiment (GRACE) water storage deficit. *Hydrol Earth Syst Sci* **25**, 511–526 (2021).

31. Tangdamrongsub, N., Ditmar, P. G., Steele-Dunne, S. C., Gunter, B. C. & Sutanudjaja, E. H. Assessing total water storage and identifying flood events over Tonlé Sap basin in Cambodia using GRACE and MODIS satellite observations combined with hydrological models. *Remote Sens Environ* **181**, 162–173 (2016).

32. Thomas, A. C., Reager, J. T., Famiglietti, J. S. & Rodell, M. A GRACE-based water storage deficit approach for hydrological drought characterization. *Geophys Res Lett* **41**, 1537–1545 (2014).

33. van Dijk, A. I. J. M. *et al.* The Millennium Drought in southeast Australia (2001-2009): Natural and human causes and implications for water resources, ecosystems, economy, and society. *Water Resour Res* **49**, 1040–1057 (2013).

34. Gerdener, H., Engels, O. & Kusche, J. A framework for deriving drought indicators from the Gravity Recovery and Climate Experiment (GRACE). *Hydrol Earth Syst Sci* **24**, 227–248 (2020).

35. Birant, D. & Kut, A. ST-DBSCAN: An algorithm for clustering spatial-temporal data. *Data Knowl Eng* **60**, 208–221 (2007).

36. Houborg, R., Rodell, M., Li, B., Reichle, R. & Zaitchik, B. F. B. F. Drought indicators based on model-assimilated Gravity Recovery and Climate Experiment (GRACE) terrestrial water storage observations. *Water Resour Res* **48**, W07525 (2012).

37. Mafaranga, H. Heavy Rains, Human Activity, and Rising Waters at Lake Victoria. *Eos (United States)* **101**, 7–9 (2020).

38. Blunden, J. & Arndt, D. S. State of the Climate in 2019. *Bull Am Meteorol Soc* **101**, S1–S8 (2020).

39. Jiménez-Muñoz, J. C. *et al.* Record-breaking warming and extreme drought in the Amazon rainforest during the course of El Niño 2015–2016. *Sci Rep* **6**, 33130 (2016).

40. Brandimarte, W. & Freitas Jr., G. Brazil's Worst Water Crisis in 91 Years Threatens Power Supplies - Bloomberg. *Bloomberg* https://www.bloomberg.com/news/articles/2021-05-28/brazil-s-worst-water-crisis-in-91-years-threatens-power-supplies (2021).

41. Williams, A. P., Cook, B. I. & Smerdon, J. E. Rapid intensification of the emerging southwestern North American megadrought in 2020–2021. *Nat Clim Chang* **12**, 232–234 (2022).

42. Horowitz, J. Europe's Scorching Summer Puts Unexpected Strain on Energy Supply. *New York Times* https://www.nytimes.com/2022/08/18/world/europe/drought-heat-energy.html (2022).

43. Rippey, B. R. The U.S. drought of 2012. *Weather Clim Extrem* **10**, 57–64 (2015).

44. Phillips, T., Nerem, R. S., Fox-Kemper, B., Famiglietti, J. S. & Rajagopalan, B. The influence of ENSO on global terrestrial water storage using GRACE. *Geophys Res Lett* **39**, L16705 (2012).

45. Pfeffer, J., Cazenave, A. & Barnoud, A. Analysis of the interannual variability in satellite gravity solutions: detection of climate modes fingerprints in water mass displacements across continents and oceans. *Clim Dyn* **58**, 1065–1084 (2022).

46. Guo, L. *et al.* Links between global terrestrial water storage and large-scale modes of climatic variability. *J Hydrol (Amst)* **598**, 126419 (2021).

47. Berg, A. & Sheffield, J. Climate Change and Drought: the Soil Moisture Perspective. *Curr Clim Change Rep* **4**, 180–191 (2018).

48. Trenberth, K. E. Atmospheric moisture residence times and cycling: Implications for rainfall rates and climate change. *Clim Change* **39**, 667–694 (1998).

49. Eicker, A., Forootan, E., Springer, A., Longuevergne, L. & Kusche, J. Does GRACE see the terrestrial water cycle "intensifying"? *J Geophys Res* **121**, 733–745 (2016).

50. Pokhrel, Y. *et al.* Global terrestrial water storage and drought severity under climate change. *Nat Clim Chang* **11**, 226–233 (2021).

51. Greve, P. *et al.* Global assessment of trends in wetting and drying over land. *Nat Geosci* **7**, 716–721 (2014).

52. Scanlon, B. R. *et al.* Effects of climate and irrigation on GRACE-based estimates of water storage changes in major US aquifers. *Environmental Research Letters* **16**, E1080–E1089 (2021).

53. Dai, A. G. & Wigley, T. M. L. Global patterns of ENSO induced precipitation. *Geophys. Res* **27**, 1283–1286 (2000).

54. Mason, S. J. & Goddard, L. Probabilistic precipitation anomalies associated with ENSO. *Bull Am Meteorol Soc* **82**, 619–638 (2001).

55. Maggioni, V. & Massari, C. (Eds.). *Extreme Hydroclimatic Events and Multivariate Hazards in a Changing Environment*. *Extreme Hydroclimatic Events and Multivariate Hazards in a Changing Environment* (Elsevier, 2019). doi:10.1016/c2017-0-02344-3.

56. Wiese, D. N. *et al.* The Mass Change designated observable study: overview and results. *Earth and Space Science* **l**, e2022EA002311 (2022).

57. Rodell, M. *et al.* The observed state of the water cycle in the early twenty-first century. *J Clim* **28**, 8289–8318 (2015).

Methods References

58. Landerer, F. W. & Swenson, S. C. Accuracy of scaled GRACE terrestrial water storage estimates. *Water Resour Res* **48**, W04531 (2012).

59. Rowlands, D. D. *et al.* Resolving mass flux at high spatial and temporal resolution using GRACE intersatellite measurements. *Geophys Res Lett* **32**, L04310 (2005).

60. Swenson, S., Yeh, P. J. F., Wahr, J. & Famiglietti, J. A comparison of terrestrial water storage variations from GRACE with in situ measurements from Illinois. *Geophys Res Lett* **33**, L16401 (2006).

61. Rodell, M. *et al.* Emerging trends in global freshwater availability. *Nature* **557**, 651–659 (2018).

62. Li, B. *et al.* Global GRACE Data Assimilation for Groundwater and Drought Monitoring: Advances and Challenges. *Water Resour Res* **55**, 7564-7586 (2019).

63. Koster, R. D., Suarez, M. J., Ducharne, A., Stieglitz, M. & Kumar, P. A catchment-based approach to modeling land surface processes in a general circulation model: 1. Model structure. *Journal of Geophysical Research: Atmospheres* **105**, 24809–24822 (2000).

64. Winter, T. C., Harvey, J. W., Franke, O. L. & Alley, W. M. *Ground Water Surface Water and A Single Resource*. *USGS Publications* (Diane Publishing, 1998).

65. Svoboda, M. *et al.* The Drought Monitor. *Bull Am Meteorol Soc* **83**, 1181–1190 (2002).

66. Li, B. & Rodell, M. Changing intensity of hydroclimatic extreme events revealed by GRACE and GRACE-FO Data sets (Version 2) [Data set]. *Zenodo*, https://doi.org/10.5281/zenodo.7599831.

66. Li, B. & Rodell, M. Changing intensity of hydroclimatic extreme events revealed by GRACE and GRACE-FO Data sets (Version 1) [Data set]. *Zenodo*, https://doi.org/10.5281/zenodo.7585390.

Extended Data Tables

Event metrics	Wet events	Dry events
Total Intensity	0.63 (12)	-0.57 (0)
Average severity	0.58 (12)	-0.74 (11)
Number of events	--	0.64 (0)
Average duration	0.47(11)	0.51 (12)
Total extent	0.60 (12)	0.43 (0)

Table ED1. Relationships between event metrics and global mean temperature. Correlation coefficients between global monthly total (sum over all events) or average metrics and global mean temperature. Lags (months) of maximum correlation are noted in parentheses. The maximum lag tested was 12 months. All correlations are significant with $\rho<0.05$.

Climate Zone	Mean TWS Anomaly (cm)	Mean duration (months)	Mean area (10^6 km^2)
Tropical	12.6	9	2.7
Dry	7.9	11	2.9
Temperate	11.5	8	1.3
Continental	8.1	14	2.7

Table ED2. Mean statistics of extreme wet events by climate zone.

Climate Zone	Mean TWS Anomaly (cm)	Mean duration (months)	Mean area (10^6 km^2)
Tropical	-12.8	9	2.3
Dry	-8.2	10	1.7
Temperate	-9.5	9	1.9
Continental	-7.6	15	2.9

Table ED3. Mean statistics of extreme dry events by climate zone.

Figures

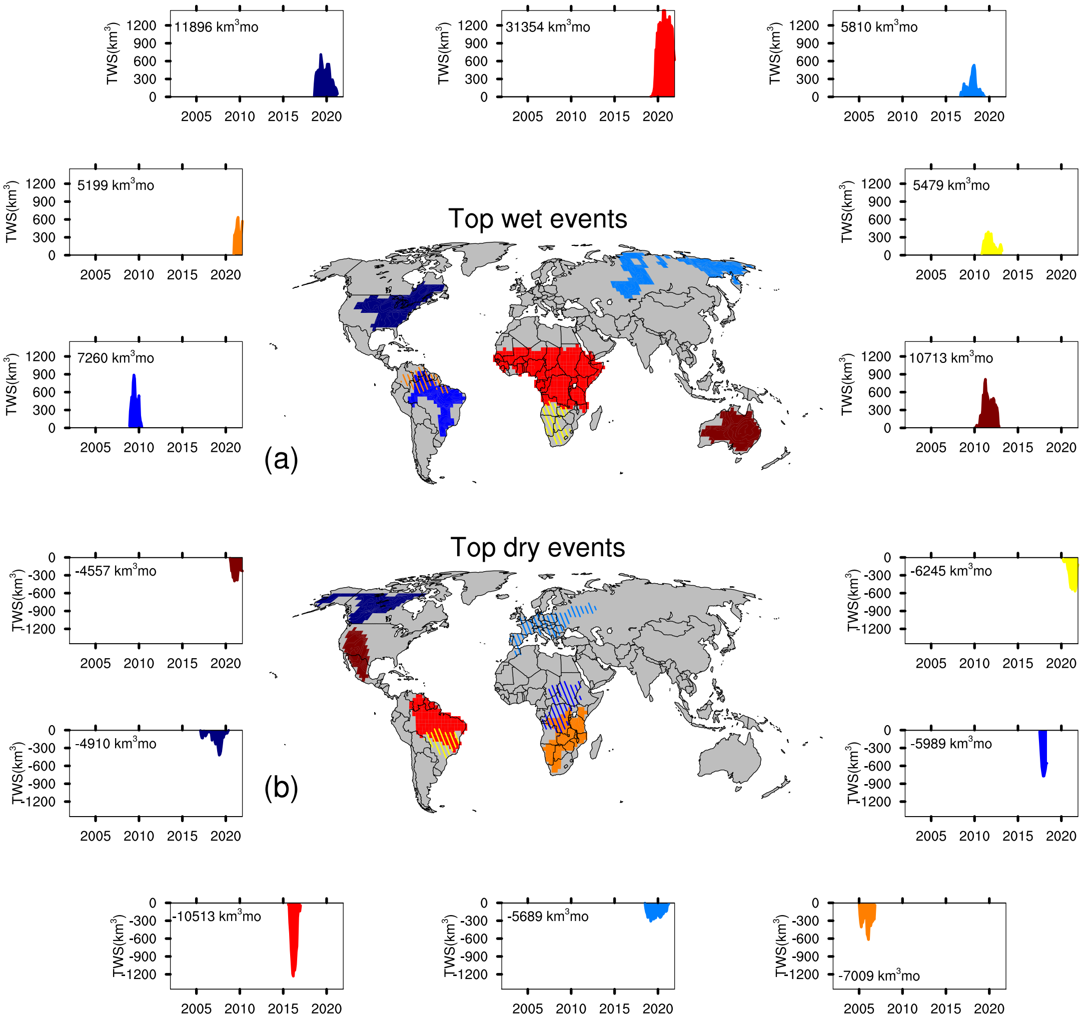
Top wet events
(a)
11896 km³mo
31354 km³mo
5810 km³mo
5199 km³mo
5479 km³mo
7260 km³mo
10713 km³mo
Top dry events
(b)
-4557 km³mo
-6245 km³mo
-4910 km³mo
-5989 km³mo
-10513 km³mo
-5689 km³mo
-7009 km³mo
TWS(km³)
2005
2010
2015
2020

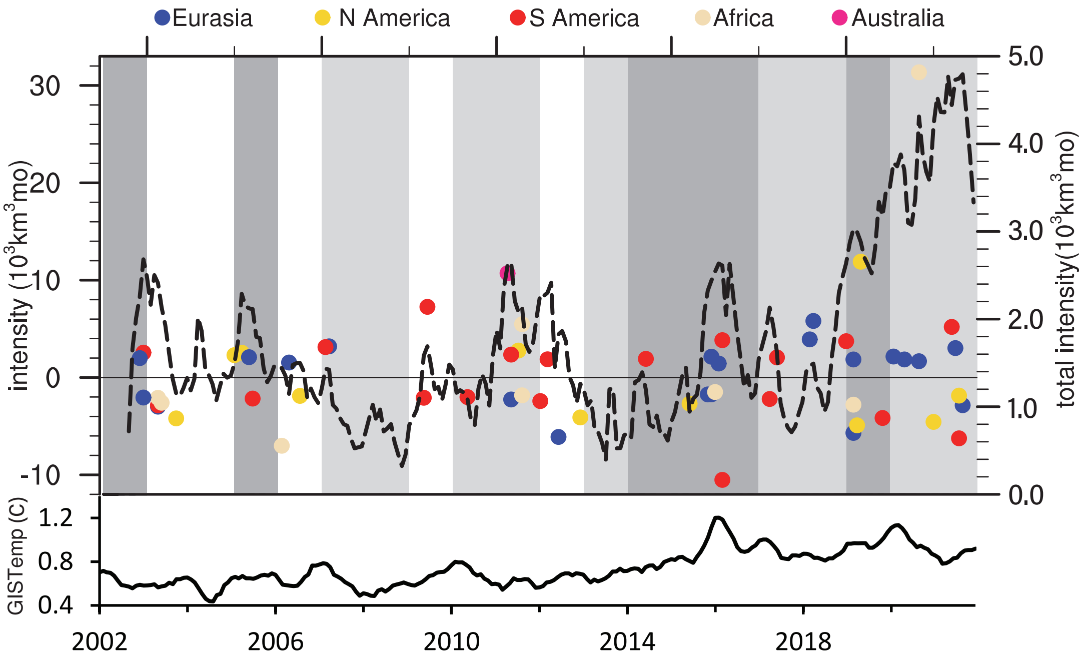

Eurasia
N America
S America
Africa
Australia
intensity (10^3km^3mo)
total intensity(10^3km^3mo)
30
20
10
0
-10
5.0
4.0
3.0
2.0
1.0
0.0
GISTemp (C)
1.2
0.8
0.4
2002
2006
2010
2014
2018

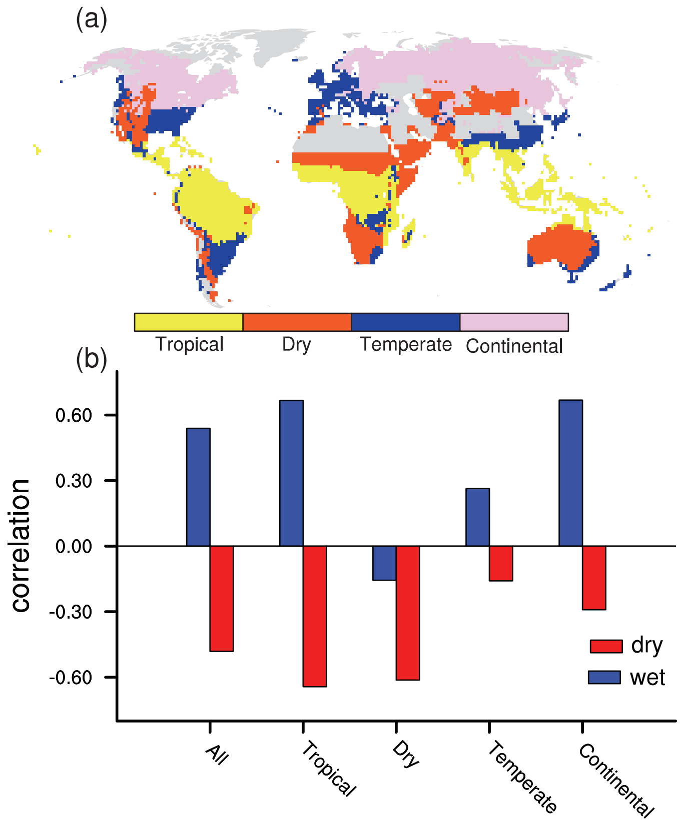
(a)
Tropical
Dry
Temperate
Continental
(b)
correlation
0.60
0.30
0.00
-0.30
-0.60
dry
wet
All
Tropical
Dry
Temperate
Continental

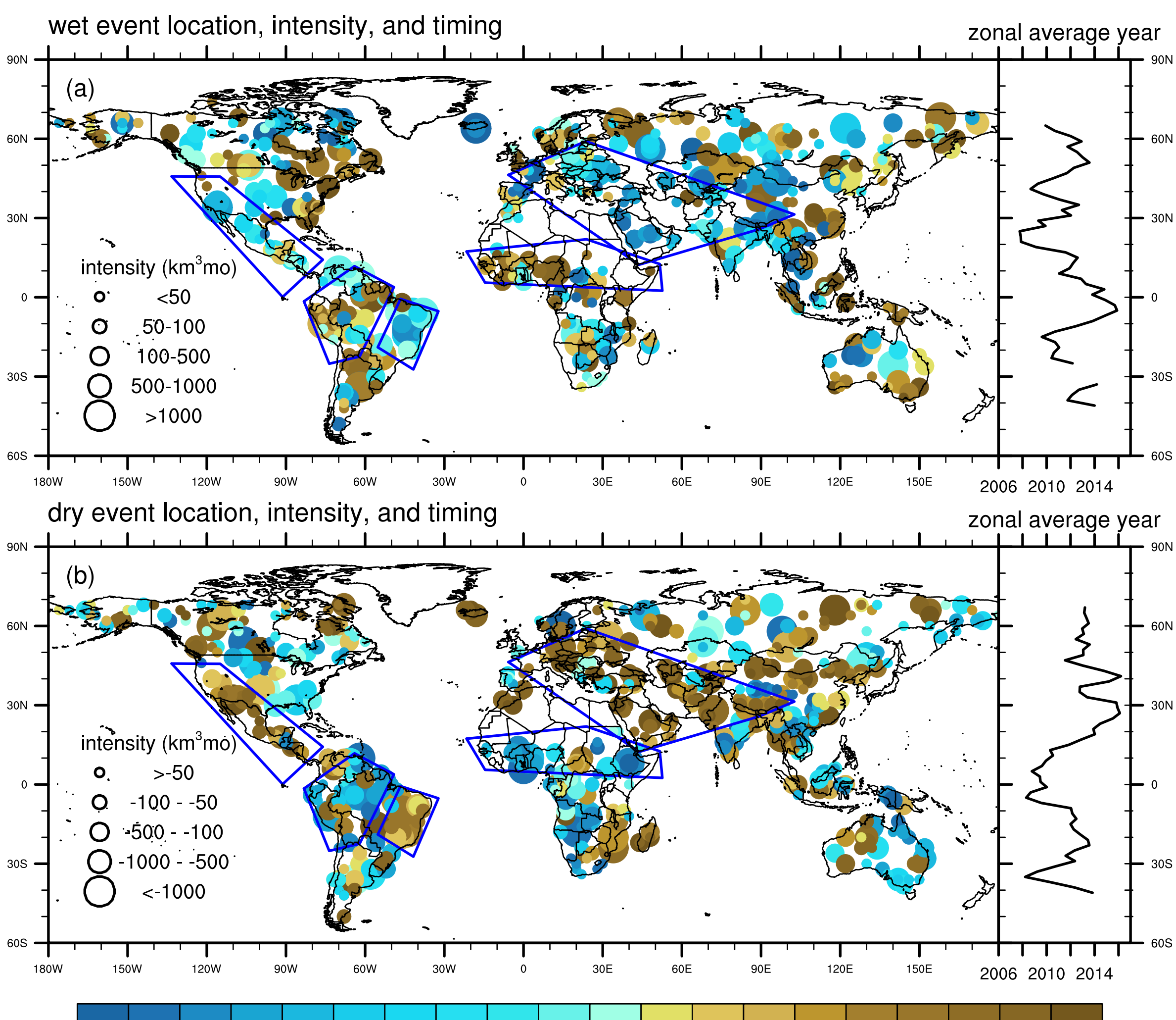
wet event location, intensity, and timing
zonal average year
(a)
intensity (km³mo)
<50
50-100
100-500
500-1000
>1000
90N
60N
30N
0
30S
60S
180W
150W
120W
90W
60W
30W
0
30E
60E
90E
120E
150E
2006
2010
2014
dry event location, intensity, and timing
zonal average year
(b)
intensity (km³mo)
>-50
-100 - -50
-500 - -100
-1000 - -500
<-1000
2002
2004
2006
2008
2010
2012
2014
2016
2018
2020

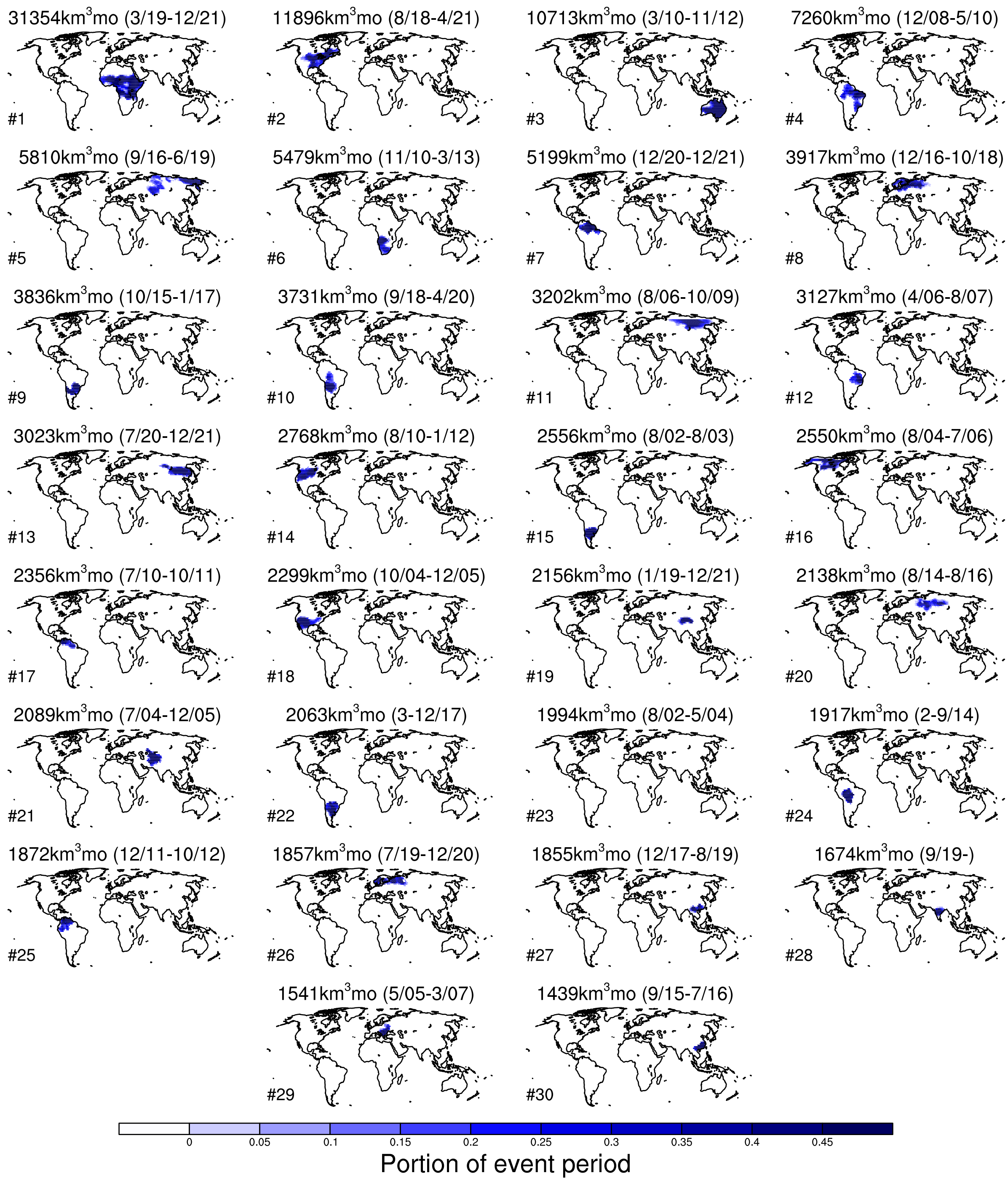
31354km3mo (3/19-12/21)
#1
11896km3mo (8/18-4/21)
#2
10713km3mo (3/10-11/12)
#3
7260km3mo (12/08-5/10)
#4
5810km3mo (9/16-6/19)
#5
5479km3mo (11/10-3/13)
#6
5199km3mo (12/20-12/21)
#7
3917km3mo (12/16-10/18)
#8
3836km3mo (10/15-1/17)
#9
3731km3mo (9/18-4/20)
#10
3202km3mo (8/06-10/09)
#11
3127km3mo (4/06-8/07)
#12
3023km3mo (7/20-12/21)
#13
2768km3mo (8/10-1/12)
#14
2556km3mo (8/02-8/03)
#15
2550km3mo (8/04-7/06)
#16
2356km3mo (7/10-10/11)
#17
2299km3mo (10/04-12/05)
#18
2156km3mo (1/19-12/21)
#19
2138km3mo (8/14-8/16)
#20
2089km3mo (7/04-12/05)
#21
2063km3mo (3-12/17)
#22
1994km3mo (8/02-5/04)
#23
1917km3mo (2-9/14)
#24
1872km3mo (12/11-10/12)
#25
1857km3mo (7/19-12/20)
#26
1855km3mo (12/17-8/19)
#27
1674km3mo (9/19-)
#28
1541km3mo (5/05-3/07)
#29
1439km3mo (9/15-7/16)
#30
0
0.05
0.1
0.15
0.2
0.25
0.3
0.35
0.4
0.45
Portion of event period

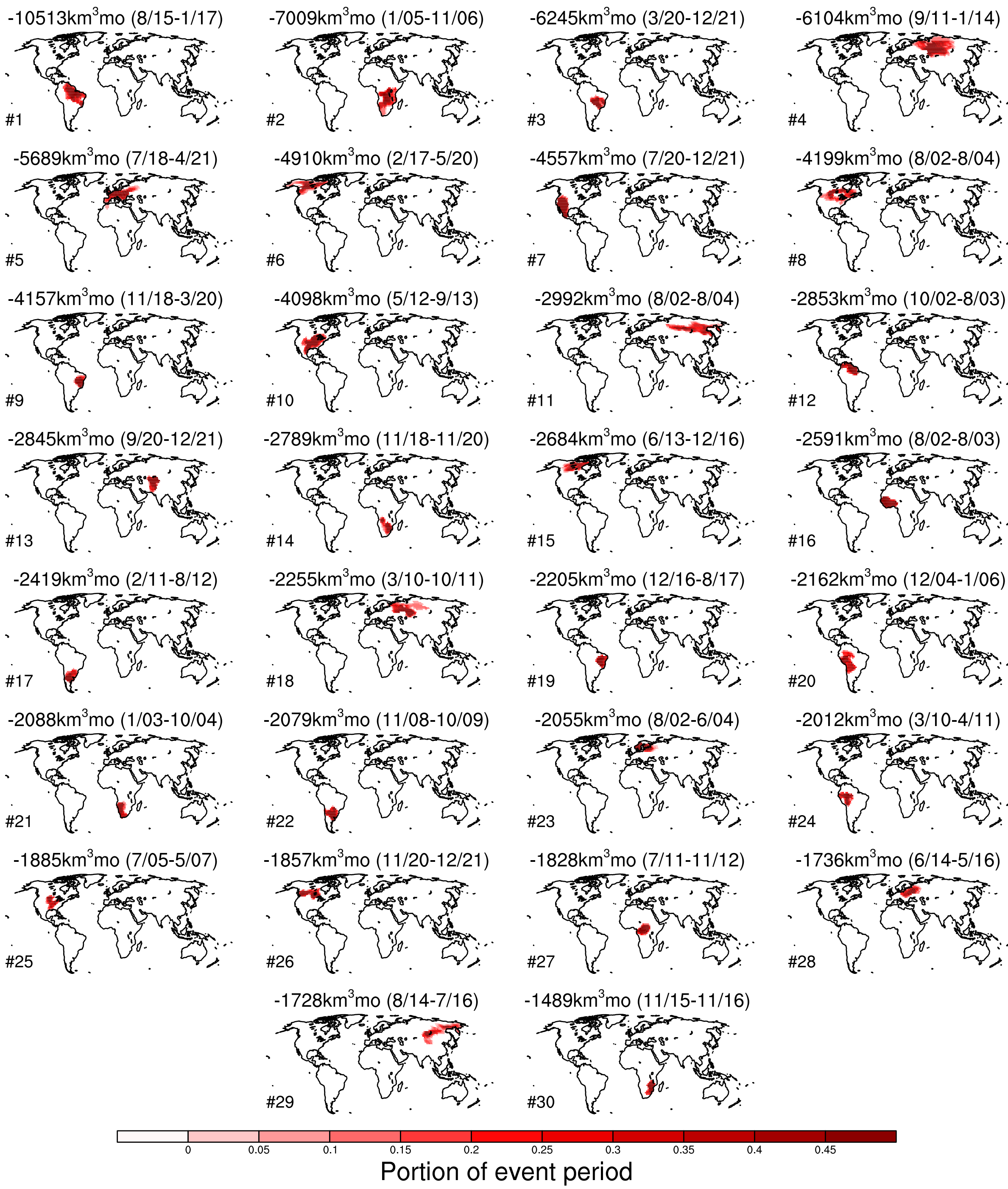
-10513km^{3}mo (8/15-1/17)
#1
-7009km^{3}mo (1/05-11/06)
#2
-6245km^{3}mo (3/20-12/21)
#3
-6104km^{3}mo (9/11-1/14)
#4
-5689km^{3}mo (7/18-4/21)
#5
-4910km^{3}mo (2/17-5/20)
#6
-4557km^{3}mo (7/20-12/21)
#7
-4199km^{3}mo (8/02-8/04)
#8
-4157km^{3}mo (11/18-3/20)
#9
-4098km^{3}mo (5/12-9/13)
#10
-2992km^{3}mo (8/02-8/04)
#11
-2853km^{3}mo (10/02-8/03)
#12
-2845km^{3}mo (9/20-12/21)
#13
-2789km^{3}mo (11/18-11/20)
#14
-2684km^{3}mo (6/13-12/16)
#15
-2591km^{3}mo (8/02-8/03)
#16
-2419km^{3}mo (2/11-8/12)
#17
-2255km^{3}mo (3/10-10/11)
#18
-2205km^{3}mo (12/16-8/17)
#19
-2162km^{3}mo (12/04-1/06)
#20
-2088km^{3}mo (1/03-10/04)
#21
-2079km^{3}mo (11/08-10/09)
#22
-2055km^{3}mo (8/02-6/04)
#23
-2012km^{3}mo (3/10-4/11)
#24
-1885km^{3}mo (7/05-5/07)
#25
-1857km^{3}mo (11/20-12/21)
#26
-1828km^{3}mo (7/11-11/12)
#27
-1736km^{3}mo (6/14-5/16)
#28
-1728km^{3}mo (8/14-7/16)
#29
-1489km^{3}mo (11/15-11/16)
#30
0
0.05
0.1
0.15
0.2
0.25
0.3
0.35
0.4
0.45
Portion of event period

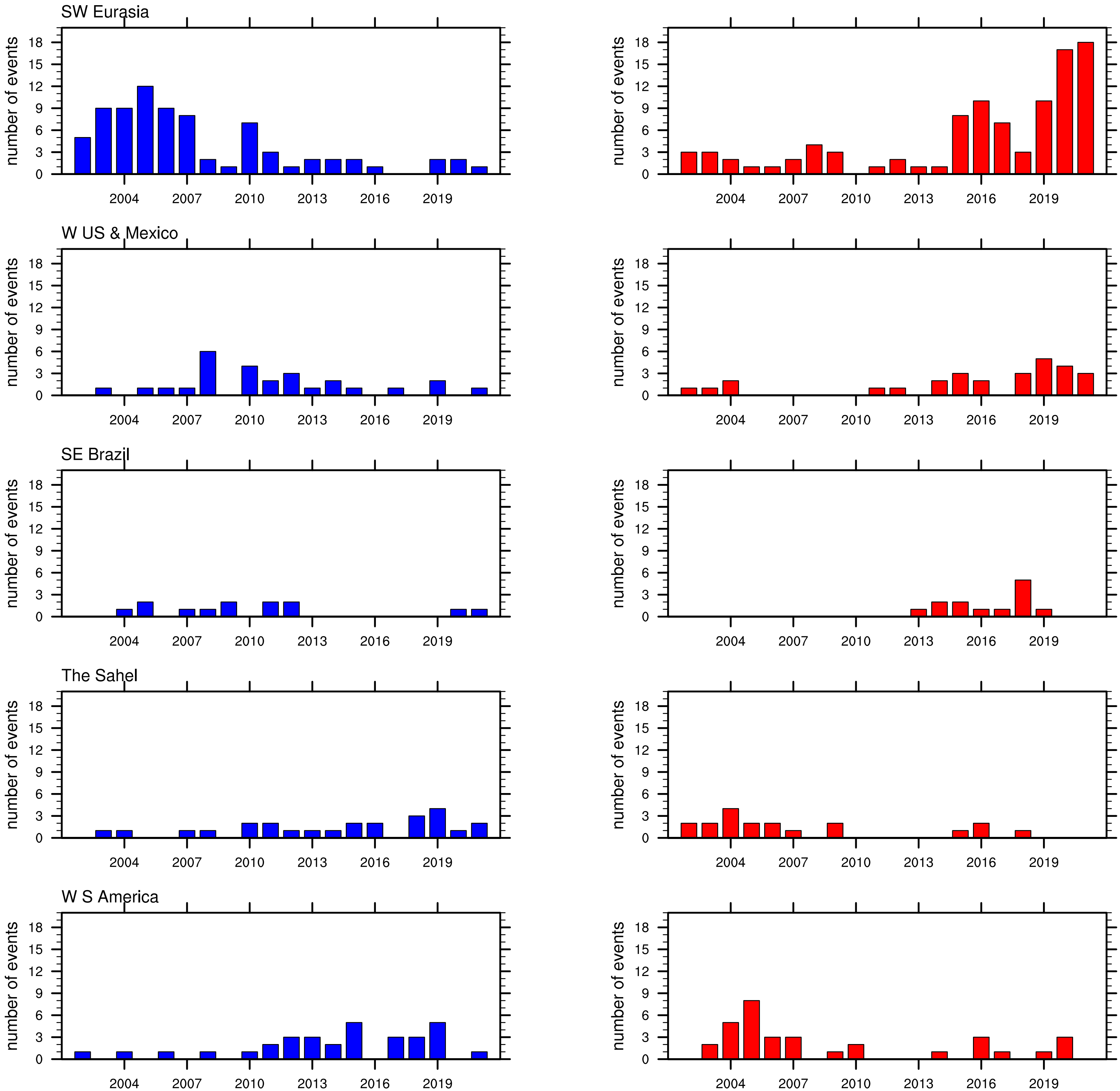
SW Eurasia
W US & Mexico
SE Brazil
The Sahel
W S America
number of events
0
3
6
9
12
15
18
2004
2007
2010
2013
2016
2019